COMPUTATIONAL FLUID DYNAMICS SIMULATION AND PERFORMANCE STUDY OF A THREE-SEPARATION COMBINED AIR CLASSIFIER

by

Chenxi HUI, Qiang LI, Jiaxiang PENG, and Ying FANG *

College of Materials Science and Engineering, Nanjing Tech University, Nanjing, China

Original scientific paper
https://doi.org/10.2298/TSCI230513183H

This paper mainly uses ANSYS-FLUENT 19.2 software to simulate the movement of the air-flow in a three-separation combined classifier. The simulation results indicate that the air-flow is uniformly distributed in the V-classifier under the action of dispersion plates and baffles. As the air-flow enters the rotor channel, the tangential velocity of the air-flow increases uniformly and remains stable in the axial direction, providing a stable centrifugal force field for particle classification. From the analysis of the flow field and particle trajectories, the separation interface between the upward path for particles and the downward path for coarse particles is relatively clear. The experimental results with sodium bicarbonate show that the V-classifier has a good pre-classification effect. The rotor cage speeds of 300 rpm and 500 rpm are the best working conditions for the coarse powder and fine powder collection, respectively. This study not only provides a new strategy for the design and development of air classifier, but also provides theoretical guidance for its application in industrial production.

Key words: *air classifier, combined air classifier, CFD, flow field, classification performance*

Introduction

Particle classification is an indispensable unit operation in powder processing and preparation. Due to the shortage of water resources and process requirements, dry classification devices are currently employed in most factories compared to wet classification. As a mainstream dry classification equipment in industrial production, the turbo air classifier is widely used in mineral separation, chemical industry, building materials, and other fields [1-3]. The structure of the vortex classifier is shown in the fig. 1(a).

With the rapid development of CFD, the numerical simulation method has been widely used to study the structural optimization of turbor air classifiers in recent years and has achieved remarkable results. Some researchers have improved the rationality and stability of the flow field by optimizing the local structures for the rotor cage [4-6], the volute [7], and the guide vane [8-10], thereby enhancing the classification performance of the turbo air classifier. For example, a new rotor cage is designed with non-radial arc blades to optimize the flow field distribution between the adjacent blades of the rotor cage [4]. The simulation results showed that the flow field distribution within the adjacent blades of the rotor cage was significantly improved. The air-flow streamlines perfectly matched the shape

* Corresponding author, e-mails: powderfang@163.com; powder8817@njtech.edu.cn

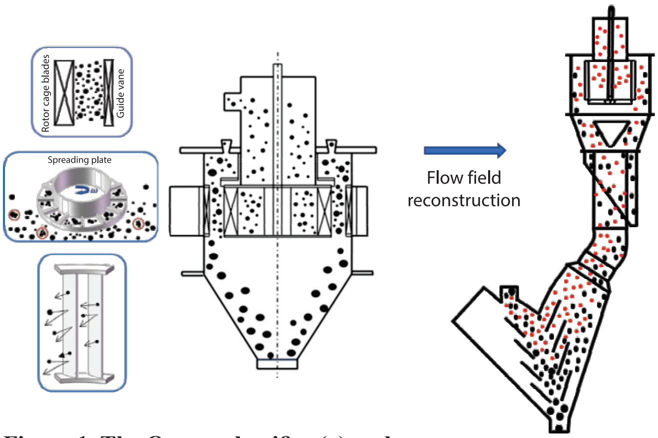

Figure 1. The O-sepa classifier (a) and the three-separation combined air classifier (b)

of the non-radial arc blades, and there was no inertial anti-vortex in the rotor cage channel. Furthermore, some researchers have also investigated the effect of operating parameters on the flow field distribution using CFD techniques and have obtained optimal operating combinations of operating parameters [11, 12].

However, with the continuous acceleration of industrial development and the surge in production demand, some problems have emerged in the industrial application of turbo air classifiers [13-17]. First of all, the annular area is a place for both material classification and dispersion, hence the dust concentration in the annular area is high, which will increase the chance of particle collision and agglomeration, resulting in a reduction in classification efficiency. Secondly, with the increasing demand for industrial capacity, if only the feeding rate is increased, it will lead to uneven distribution of materials on the spreading plate and the formation of thicker material curtains alternating with material-free voids in the annular zone, which is adverse to material classification [15]. Although some researchers have addressed this problem by increasing the number of feeding ports, replacing the single-layer spreading plate with the double-layer spreading plate, and other methods, it has not been fundamentally solved due to the structural limitations of the classifier itself [18]. Furthermore, since the asymmetry of the classifier structure and air supply, regions of too large and too small air velocity appear at the intersection of the air inlet and volute. This phenomenon will lead to an unstable classification flow field and local ash deposition [19, 20], while it will cause serious wear to the guide vane [16]. To fundamentally solve the aforementioned problems, Jia *et al.* [21] designed and studied a new high-efficiency rotor classifier. Mou *et al.* [22] and Li *et al*. [23] optimised its internal structure by numerical simulation and mentioned a combined static classifier and high-efficiency rotor classifier. However, there are no studies on the internal flow field and particle motion of combinatorial classifiers.

In this paper, the particle motion and classification mechanisms of a three-separation combined classifier are investigated by CFD simulations and combined with design principles. The turbulent Reynolds stress model (RSM) and the multi-reference frame model (MRF) are also used to simulate the air-flow in the three-separation combined classifier to study the internal flow field characteristics of the classifier. In addition, the effect of rotor speed on the three-separation combined air classifier is investigated by material experiments.

Calculation methodology

Description of the equipment

The three-separation combined air classifier, consisting of a V-classifier and a dynamic rotor classifier, was designed with the two vital aspects of material dispersion and classification in full consideration, the 3-D structure is shown in fig. 2. For the convenience of expression, the three-separation combined air classifier is denoted as the TSC classifier. The V-classifier, a static classifier without any moving components, could product generally a cut size in the range of 80-1500 μm [24]. Its main function in the TSC classifier is to initially pre-classification and disperse the material, and the pre-treated material reports to the dynamic rotor classifier part for further processing. However, the TSC classifier could generate a finer cut size in the range of 20-150 μm, indicating that the dynamic rotor classifier is the main place for material classification and has much better classification performance.

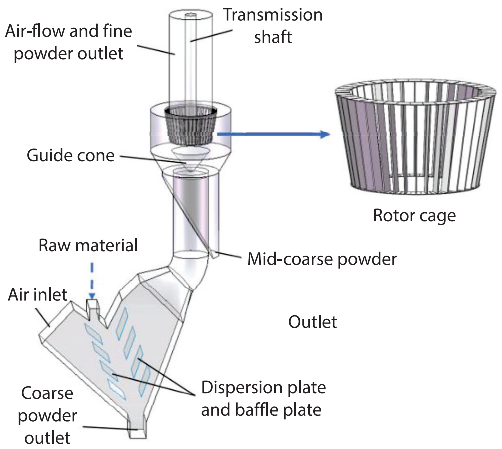

Figure 2. The 3-D structure of the TSC classifier

The working principle of the TSC classifier is raw materials are fed into the TSC classifier through the feeding port for the V-classifier. In the V-classifier part, the materials are fully dispersed under the action of dispersing plates and baffles. The coarser particles report to the coarse fraction by the bottom discharge port, and the remaining materials enter the dynamic rotor classifier part with the air-flow. When the air-flow carries the material to the guide cone, the material will hit the guide cone due to inertia for further dispersion. As the air-flow path has a large deflection before entering the rotor cage, part of the coarse particles move towards the cylinder wall due to inertia, thus hitting the cylinder wall to lose speed, settling along the cylinder wall under the action of gravity, and being collected to the medium-coarse fraction. The rest of the material enters the classification area formed by the rotor cage with the air-flow, and at this time, the particles are mainly affected by the air-flow drag force, centrifugal force, and gravity. These three forces determine whether the particles are collected to the medium-coarse or the fine fraction. Based on this process, the raw materials are finally separated into three fractions: coarse powder, medium-coarse powder, and fine powder.

Model establishment and mesh generation

SolidWorks and ICEM were employed to model and mesh the TSC classifier, respectively. The model is mainly divided into seven parts, including the V-classifier part, connecting pipe, medium-coarse powder outlet part, cone, classification chamber, rotor cage, and air-flow outlet. The main dimensions of the model are the ratio of the upper and lower diameters for the rotor cage with a height of 150 mm is 1:0.8, where the upper diameter is 260 mm and the lower diameter is 208 mm. The 36 blades with a thickness of 2 mm and a length of 20 mm are evenly distributed on the rotor cage circumference. The diameter of the classification room is 400 mm and the height is 210 mm. The height and diameter of the guild cone are 103 mm and 188 mm, respectively. The dispersing plate and baffle are installed at an angle of 80°, and both lengths are 112 mm. The size of the air inlet is 130 mm × 150 mm with an inclination angle of 35°.

The unstructured mesh was used for the medium-coarse powder outlet, and the structured mesh is used for the rest, meshes of the TSC classifier is indicated in fig. 3(a). Before the simulation, the mesh independence test was conducted, and four different mesh numbers were checked including 1512927, 2236106, 2860418, and 3489680. The radial velocity distributions on the outer surface of the rotor cage were obtained using these four different mesh numbers, as show in fig. 3(b). As can be seen in this picture, when the number of meshes reaches 2860418, the radial velocity distribution is almost unchanged, indicating that the mesh independence requirement is met [25]. Thus, 2860418 meshes are selected to simulate the classifier in this study.

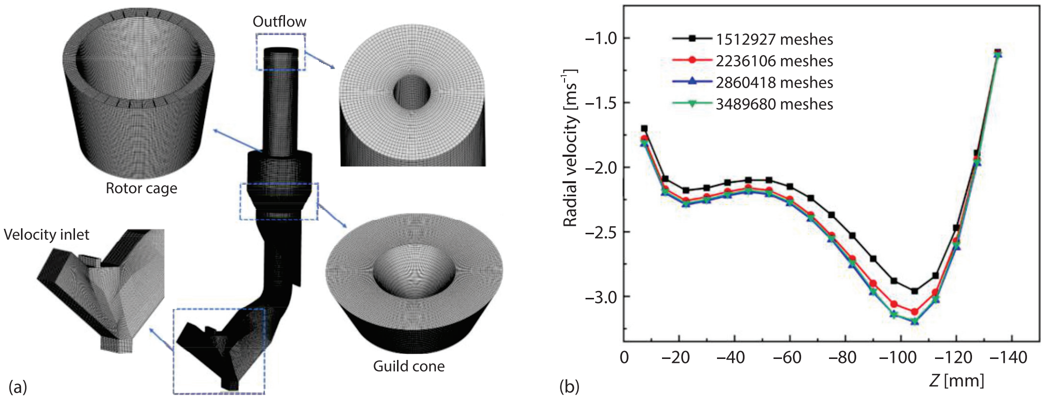

Figure 3. Meshes of the TSC classifier (a) and radial velocity distribution for different mesh numbers (b)

Turbulence model and simulation conditions

In this paper, ANSYS FLUENT 19.2 was adopted for the 3-D steady simulation. For incompressible air-flow, the mass and momentum equations are expressed:

$$\frac{\partial u_i}{\partial x_i} = 0 \tag{1}$$

$$\rho u_j \frac{\partial u_i}{\partial x_j} = -\frac{\partial p}{\partial x_i} + \frac{\partial}{\partial x_j}\left[u\left(\frac{\partial u_i}{\partial x_j} - \frac{\partial u_j}{\partial x_i}\right)\right] - \rho\frac{\overline{\partial u_i' u_j'}}{\partial x_j} \tag{2}$$

where ρ is the gas density, u_i – the fluid velocity, x_i – the position, μ – the gas viscosity, p – the static pressure, and

$$-\rho\frac{\overline{\partial u_i' u_j'}}{\partial x_j}$$

refers to the Reynolds stress term.

The RSM has been proved to be a suitable model for describing the anisotropic flow in air classifiers. It can accurately predict the turbulence structure and pressure drop inside air classifiers [25, 26]. The transport equation for the Reynolds stress can be given:

$$\frac{\partial}{\partial t}\left(\rho\overline{u_i u_j}\right) + \frac{\partial}{\partial x_k}\left(\rho U_k \overline{u_i u_j}\right) = D_{ij} + G_{ij} + \varphi_{ij} - \varepsilon_{ij} \tag{3}$$

$$D_{ij}=-\frac{\partial}{\partial x_k}\left(\rho\overline{u_k u_i u_j}+\overline{pu_j}\delta_{ik}+\overline{pu_i}\delta_{jk}-\mu\frac{\partial}{\partial x_k}\overline{u_i u_j}\right) \tag{4}$$

$$G_{ij}=\rho\left(\overline{u_i u_k}\frac{\partial U_j}{\partial x_k}+\overline{u_j u_k}\frac{\partial U_i}{\partial x_k}\right) \tag{5}$$

$$\varphi_{ij}=\overline{p\left(\frac{\partial u_i}{\partial x_j}+\frac{\partial u_j}{\partial x_i}\right)} \tag{6}$$

$$\varepsilon_{ij}=2\mu\frac{\partial u_i}{\partial x_k}\frac{\partial u_j}{\partial x_k} \tag{7}$$

The two terms on the left side of eq. (3) are the time change rate of the Reynolds stress and convection term, respectively. The four terms on the right are the diffusion term, stress generation term, pressure strain term, and turbulent dissipation term. The diffusion term, D_{ij}, appears as divergence with conservation. It consists of the viscous diffusion term, pressure diffusion term, and turbulent diffusion term. The stress generation term, G_{ij}, denotes the interaction between the mean flow gradient and Reynolds stress. For incompressible flows, G_{ij} = 0. The pressure strain term, φ_{ij}, also known as Reynolds stress redistribution term, consists of the turbulent strain and turbulent pressure. The fluid viscosity coefficient and turbulent velocity gradient constitute the turbulent dissipation term, ε_{ij}, whose principal function is to consume turbulent energy.

The wall boundary is treated with no-slip boundary conditions and the near-wall surface with standard wall functions. The moving rotor cage inside the dynamic rotor classifier part is simulated using the MRFM. The rotor cage speed is set to 500 rpm, with a clockwise rotation direction. The SIMPLEC algorithm is adopted for the pressure-velocity coupling, and the QUICK difference scheme is used for the convection and diffusion. The boundary condition for the air inlet is defined as *velocity-inlet* and that for the air outlet is *outflow*.

Discrete phase model

In the discrete phase simulation, the particle trajectory was obtained by steady-state tracking of the discrete phase model. In this steady-state approach, when the continuous phase iteration achieves convergence and the flow field reaches a steady-state, the trajectory of each particle from the starting position its ending position is integrated one by one. Under the condition of a continuous phase flow field at a certain time, the particle state in a series of integration time steps can be obtained in a steady-state way. The series of particle positions can be connected into a motion trajectory. The steady-state tracking method is suitable for single-phase coupling calculations, which is used to add discrete phase particles and calculate the trajectory after getting the stable flow field. The particle motion equation is expressed:

$$\frac{\mathrm{d}\vec{u}_P}{\mathrm{d}t}=F_D\left(\vec{u}-\vec{u}_P\right)+\vec{\mathrm{g}}\frac{\left(\rho_P-\rho\right)}{\rho_P} \tag{8}$$

where $\vec{u}_p$ is the particle velocity, t – the time, $\vec{u}$ – the gas velocity, $\vec{\mathrm{g}}$ – the gravitational acceleration, ρ_p – the particle density, ρ – the fluid density, and F_D – the drag force, derived by:

$$F_D = \frac{18\mu}{\rho_P D_P^2} \frac{C_D \mathrm{Re}_P}{24} \tag{9}$$

$$\mathrm{Re}_P = \frac{\rho D_P \left|\vec{u}_P - \vec{u}\right|}{\mu} \tag{10}$$

where μ is the molecular viscosity of the gas, D_P – the particle diameter, C_D – the drag coefficient, and Re_P – the relative Reynold number.

Experiment preparation

Experimental set-up and material

The experimental classification system is composed of a TSC classifier, cyclone, bag dust collector, induced draft fan, and control system. The main classification experimental devices are shown in fig. 4(a). The raw material was sodium bicarbonate collected from the Alexa trona project in Inner Mongolia, with a density of 2159 kg/m^3. The experimental material was sampled using conical and quadratic methods, and representative samples were used for experiments. The JJS-200 standard laboratory sieve was used to analyze the particle size of the material before and after classification. The particle size distribution of the raw material is indicated in fig. 4(b), which presents that 27.5% of the powder is greater than 270 μm, 18.2% is between 150-270 μm, 22.2% is between 75-150 μm, and 32.1% is less than 75 μm (note that the product size requirements of factory are: coarse products ≥150 μm, medium-coarse products = 75~150 μm, and fine products ≤75 μm).

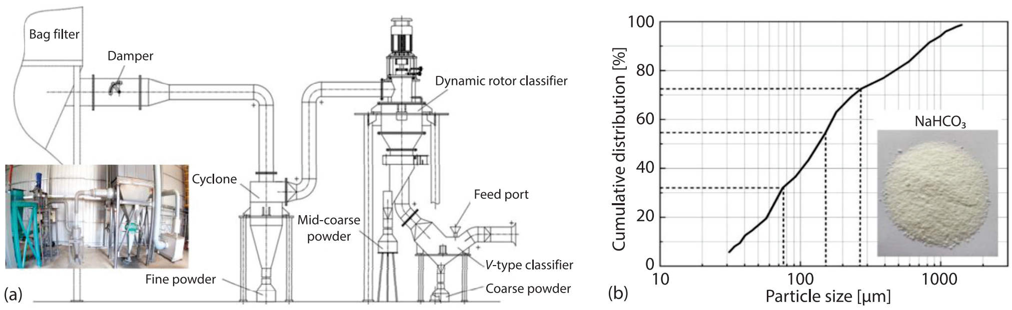

Figure 4. Schematic of the experimental set-up (a) and particle size distribution of the raw material (b)

Classification performance indexes

The recovery rate is the most commonly used classification performance index in industrial production. The fine powder recovery rate, η_C, also known as the powder selection efficiency, refers to the mass ratio of qualified particles in the fine fraction the qualified particles in the raw material. The coarse powder recovery rate, η_B, is the mass ratio of unqualified particles in the coarse fraction unqualified particles in the raw material.

The cut size d_c is the particle size at a partial classification efficiency of 50%. The classification accuracy K is expressed as the ratio of particle size with partial classification efficiency of 25% and 75%, and the larger the K-value is, the better the classification performance is.

Simulation results and analysis

Overall flow field distribution

The air-flow motion pathlines in the TSC classifier are captured, as shown in fig. 5. The air-flow enters the TSC classifier from the air inlet at the V-classifier part. When the air-flow passes through the static classifier, the air-flow is more evenly distributed in the channel due to the presence of the dispersion plates and baffles, as shown in fig. 3(c). In the V-classifier, the material is fully dispersed in the air stream by the dispersion plates and baffles, which lays the foundation for efficient classification in the subsequent dynamic classifier [27, 28]. Then the air-flow enters the dynamic rotor classifier part. Different from the conventional turbo air classifiers, the air-flow does not fill the whole classification chamber, but turns upward along the guide cone into the rotor cage, and then leaves the classifier. Due to the symmetry of the structure, the air-flow is also symmetrical about the *Z*-axis in the dynamic rotor classifier part, making the flow field evenly distributed in the circumferential direction, so that the same particles are subjected to the same force in each section, which offers a greater possibility for improving the classification performance.

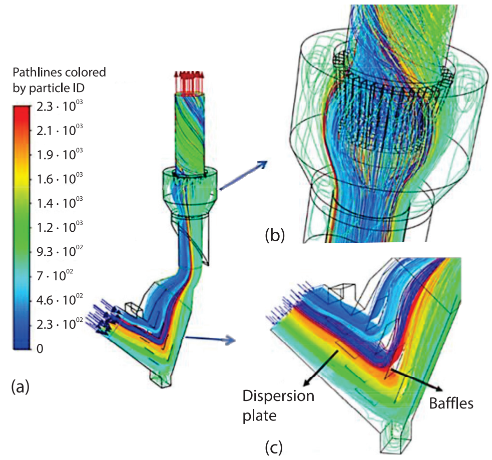

Figure 5. Air-flow pathlines in the TSC classifier

Figure 6(a) shows a vortex with a small velocity is formed near the cylinder wall, which can elutriate the settled coarse powder. In addition, almost vertical vortexes are generated at the bottom of the rotor cage (note that horizontal vortexes are required in the classification flow field), which cannot be completely eliminated because it is caused by structural dead space, but it can be weakened through structural improvements. There is a guide cone directly below the rotor cage. Its function is to evenly guide the air-flow into the classification chamber to avoid the unreasonable air-flow pathlines caused by the air-flow moving to the cylinder wall. The second is that due to the existence of the guide cone, the material will hit the guide cone under the action of inertia to get further dispersion.

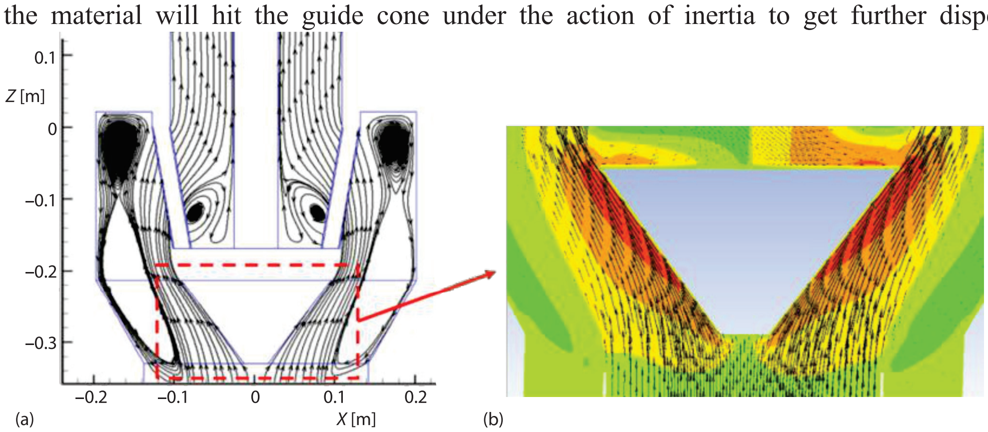

Figure 6. Air-flow movement in the dynamic rotor classifier part

Velocity distribution in the dynamic rotor classifier part

The dynamic rotor classifier is the main part of the TSC classifier and the major place for material classification, hence it is necessary to analyze its velocity field.

The tangential air-flow velocity reflects the intensity of air-flow rotation, which in turn determines the size of the centrifugal force on the particles. In the dynamic rotor classifier, the high speed rotation of the rotor cage provides tangential velocity to the flow. Figure 7 illustrates the variation of the tangential velocity of the air-flow with rotor speed. As the rotor speed increases, the tangential velocity of the classification chamber remains constant, while the tangential velocity inside the rotor gradually increases. It can be observed that the tangential velocity increases from the rotor inlet and increases uniformly in the rotor blade channel as the speed increases, as shown in the partial enlargement in fig. 7. It may be due to the rotor rotation gives a tangential acceleration the air-flow, the air-flow enters the rotor cage from axial motion radial motion, and the axial velocity is converted to radial velocity. At the same time, the air viscosity is smaller. In addition, the tangential air-flow velocity at the rotor cage edge is small and much smaller than the linear velocity for the rotor cage edge. For example, when the rotor cage speed is 500 rpm, the average linear velocity for the rotor cage edge is 6.1 m/s,

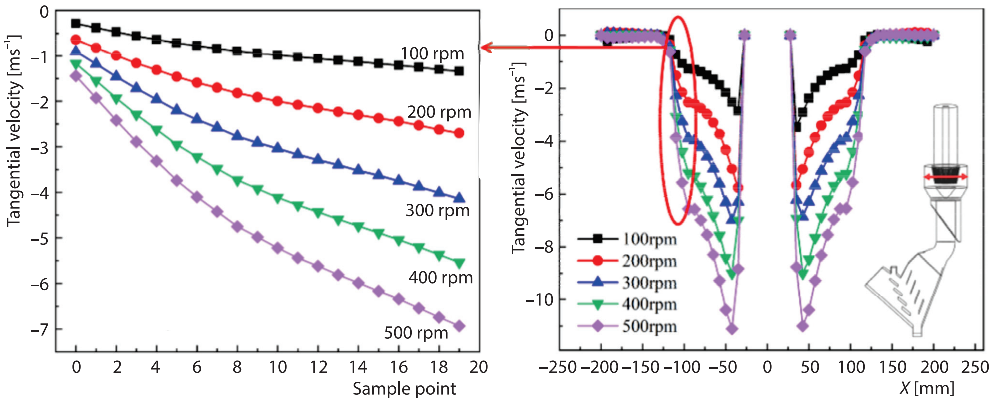

Figure 7. Tangential velocity distribution of the dynamic rotor classifier at $Z = 0$ section

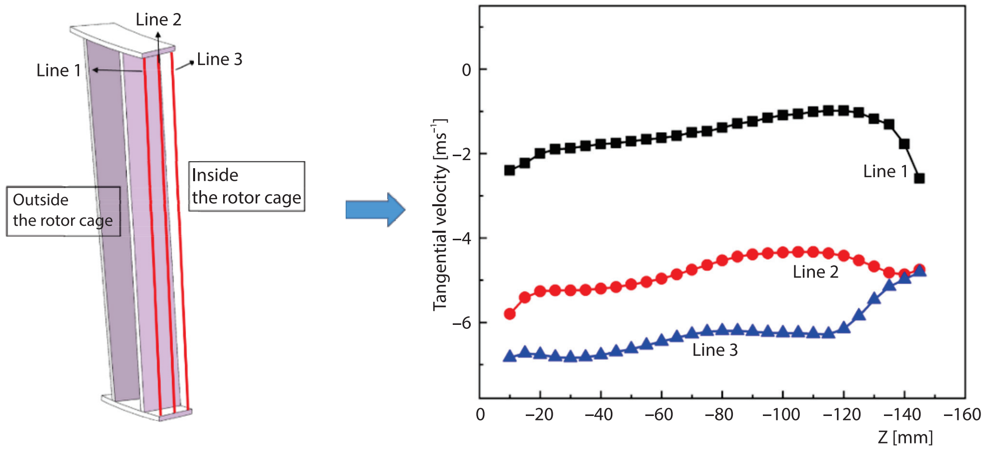

Figure 8. The tangential velocity at different positions in the rotor cage channel

while the tangential air-flow velocity is only about 1.5 m/s. This is because of the extremely low viscosity of the air, which allows the air-flow to move with lag under the drive of the rotor cage. We took points at different locations within the rotor cage channel to obtain the tangential air-flow velocity distribution in the axial direction, as shown in fig. 8. The tangential velocity at different axial positions remains stable and the velocity variation is small, indicating that a stable centrifugal force field is generated, which is conducive to the high-efficient classification of materials [22, 29].

As can be seen from fig. 9, the air-flow mainly does axial motion in the area of the classification chamber and rotor cage, resulting in a high overall axial velocity. Note that the axial velocity near the guide cone and the rotor cage is positive, while the axial velocity near the cylinder wall is negative, and there is a clear interface with zero velocity formed in between. We define the positive region near the rotor cage and the guide cone as Region I and the negative region near the cylinder wall as Region II. The Region I is the path for the particles carried by the air-flow up into the classification area, and the Region II is the path for the coarse particles to settle.

It can be seen from fig. 9(c) and fig. 9(d), with the change of the inlet air velocity and rotor cage speed, the axial velocity near the cylinder wall is between –0.4 m/s and –1.2 m/s, which is contributed to the settlement and discharge of the coarse particles. In ad-

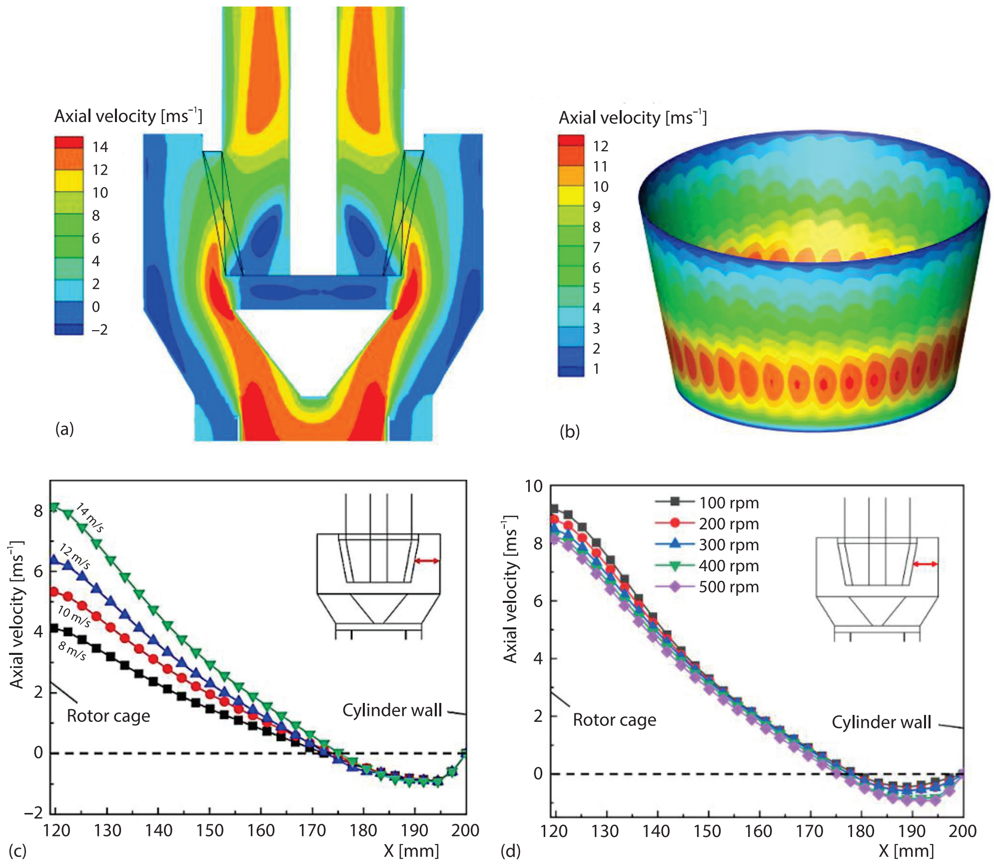

Figure 9. The axial velocity distribution

dition, the interface between the Regions I and II (where the axial velocity is zero) is located approximately 25 mm from the cylinder wall, and its position shifts slightly with the change of operating parameters. The axial velocity on the outer surface of the rotor cage reaches a maximum of 12 m/s, thereby ensuring the rapid discharge of the fine particles, as shown in fig. 9(b).

As the air-flow enters the rotor cage, the axial motion gradually transformed into radial motion, hence the radial velocity increases in the rotor cage zone, as shown in fig. 10. Note that the radial velocity at the bottom of the rotor cage is relatively small, indicating that the air-flow mainly enters the rotor cage from the middle and upper part of the rotor cage, which is caused by the vortex obstruction at the bottom of the rotor cage.

Figure 10(b) illustrates the radial velocity distribution on the outer surface of the rotating cage. The radial velocity on the outer surface of the rotor cage varies between 0.5 m/s and –5 m/s, which is significantly less than the axial velocity. Due to the blocking effect, the radial velocity is the maximum between the rotor cage blades and the minimum at the blade edges.

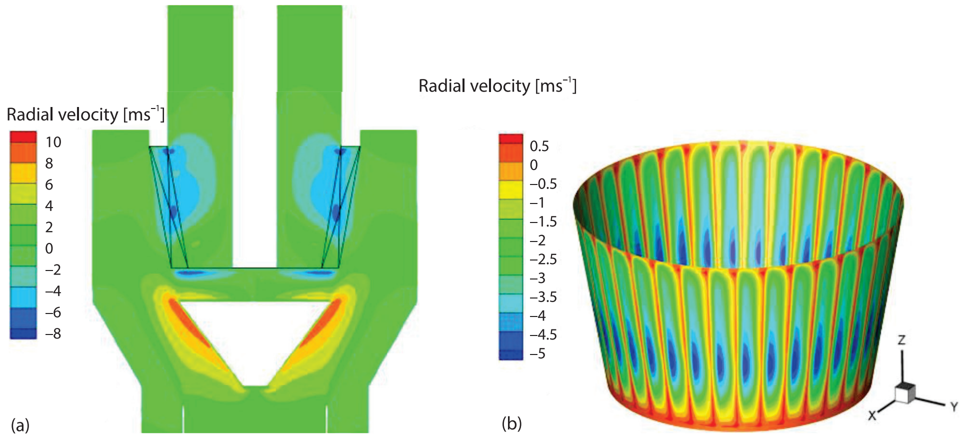

Figure 10. The radial velocity distribution

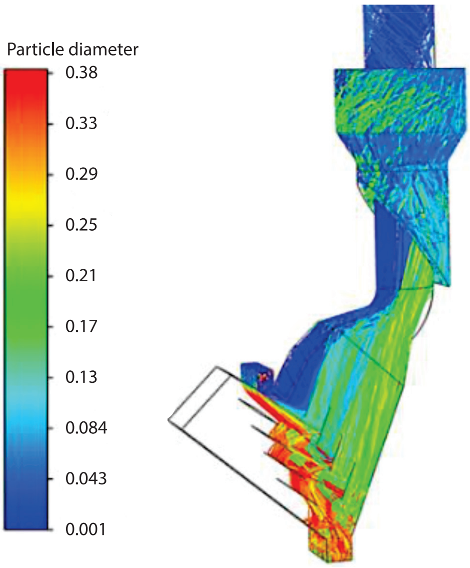

Figure 11. Particle motion trajectory

Analysis of classification mechanism

In the particle classification process, the particle motion trajectory is visualized to reveal the particle motion process, thus explaining the classification mechanism of particles. Therefore, the discrete phase model (DPM) was developed to simulate particle trajectories.

In TSC classifier, the motion of particle group is simulated by DPM model. The particles enter through the inlet of the static classifier and the particle trajectory obtained from the simulation is shown in fig. 11. It is clear from the diagram that in the static classifier section, the material particles repeatedly impact the dispersing plates and baffles, this repeated cascading movement can on the one hand fully disperse the material; on the other hand, the coarser particles can be separated out, namely, the majority of the

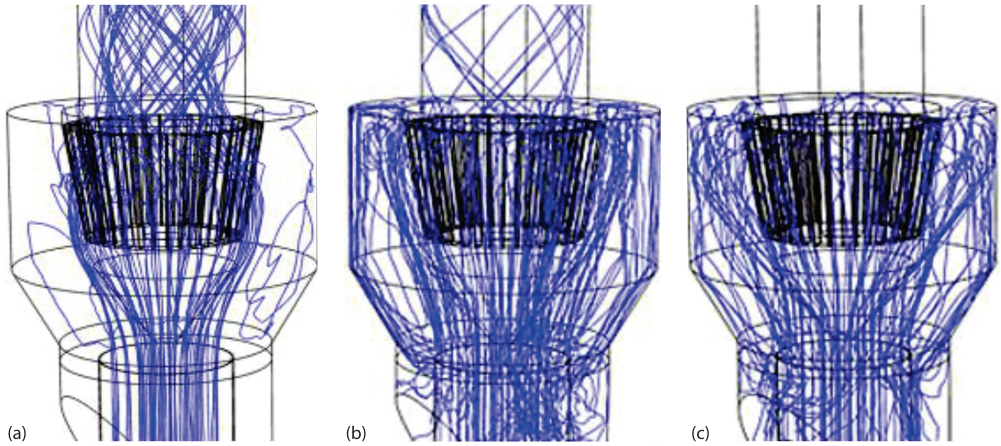

Figure 12. Trajectory of particles in dynamic rotor classifier; (a) 5 μm, (b) 32 μm, and (c) 70 μm

larger particles in red in the diagram are collected as coarse powder at the discharge port of the V-classifier. The number of large particles entering the dynamic rotor classifier is significantly reduced, which effectively reduces the dust concentration in the dynamic rotor classifier and reduces the load and wear on the dynamic rotor classifier. After dispersion and pre-classification the material enters the dynamic rotor classifier section for further classification.

To further understand the classification principle of the dynamic rotor classifier, the trajectories of the three particle size groups were simulated, as shown in fig. 12. The trajectory and force for particles of different sizes in the dynamic rotor classifier are indicated in fig. 13. In the figs. 12(a)-12(c) are the trajectories for particles with diameters, D, of 5 μm, 32 μm, and 70 μm, respectively. When the particle for D = 5 μm enters the Region I of the classification chamber, owing to its small particle size, the radial drag force is greater than the centrifugal force and coupled with the axial drag force, so that the particle is brought into the rotor cage under the combined force and collected as the fine powder. For the 32 μm particle, after entering the classification chamber, the centrifugal force is greater than the radial drag force, hence it continues to move upward under the combined force, enters the Region II of the classification chamber, settles along the cylinder wall by the gravity, and are finally collected as the medium-coarse powder. The particle for D = 70 μm is subjected to a larger reverse radial drag force due to its larger particle size, hence it enters the Region II under the combined force after passing through the guide cone. Then the particle hits the cylinder wall, loses kinetic energy, settles, and is also collected as the medium-coarse powder.

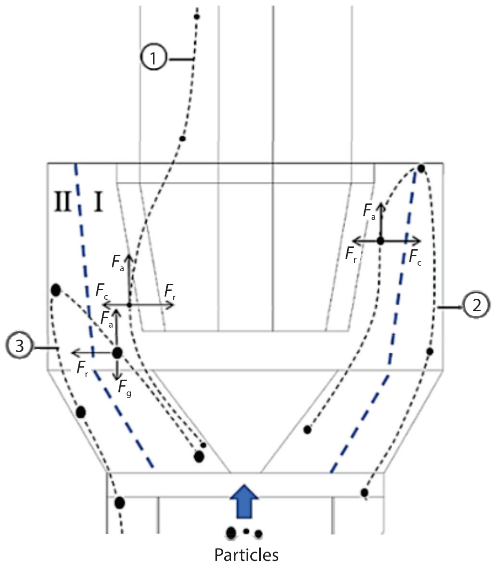

Figure 13. The trajectory, ①-③ and force for particles of different sizes; *F_a – axial force, F_r – radial drag force, F_c – centrifugal force, and F_g – gravity*

From the analysis of the axial air-flow velocity and particle trajectory, the interface between the upward path for particles and the downward path for coarse particles remains clearer, which effectively avoids the interaction between upward particles and downward particles.

Experimental results and analysis

To investigate the effect of speed on classification performance and the pre classification effect of the static classifier, the dynamic classifier rotor speed was set at 100 rpm, 200 rpm, 300 rpm, 400 rpm, and 500 rpm, respectively. The system air volume was 500 m^3 per hour and the feeding speed was 500 g per minute. The coarse fraction is collected by the V-classifier part in the experimental process, and the medium-coarse fraction is collected by the discharge port of the dynamic rotor classifier part. The fine fraction is collected by the cyclone. When calculating the recovery rate, the coarse fraction and the medium-coarse fraction are mixed as the total coarse fraction.

The results of the calculation of the particle size distribution at different speeds are illustrated in tab. 1 (note that according to the product particle size requirements of the factory, the recovery rate of coarse powder is 150 μm and that of fine powder is 75 μm). In the table, since the system air volume remains unchanged, there is little effect on the particle size composition for the coarse powder collected by the V-classifier part at different rotor cage speeds. In the coarse powder collected by the V-classifier, the average percentage of particles larger than

Table 1. The particle size composition and recovery rate after classification

n [min^{-1}]	Material sample	Particle size distribution [%]				η_B [%]	η_C [%])
		≥270 μm	150~270 μm	75~150 μm	≤75 μm		
100	Coarse fraction	91	8.3	0.7	0		
	Med-coarse fraction	68.8	19.7	10	1.5		
	Total coarse fraction	76.2	15.9	6.9	1	52.8	99.2
	Fine fraction	8.1	21.2	27.4	43.3		
200	Coarse fraction	89.6	9.6	0.8	0		
	Med-coarse fraction	73.5	16.9	8.2	1.4		
	Total coarse fraction	78.5	14.9	5.7	0.9	72.3	99.1
	Fine fraction	2.1	17.5	32.6	47.8		
300	Coarse fraction	89.2	9.7	1.1	0		
	Med-coarse fraction	61.2	30.3	7.1	1.4		
	Total coarse fraction	71.2	23.8	4.1	0.9	90.5	98.6
	Fine fraction	0	7.7	29.5	62.8		
400	Coarse fraction	82.1	15.4	2.5	0		
	Med-coarse fraction	39.2	34.6	23.9	2.3		
	Total coarse fraction	53.1	28.7	16.7	1.5	96.9	97.3
	Fine fraction	0	3.1	24.5	72.4		
500	Coarse fraction	85.5	12.7	1.8	0		
	Med-coarse fraction	36.2	27.5	30.4	5.9		
	Total coarse fraction	52.5	22.8	20.8	3.9	99.4	91.8
	Fine fraction	0	0.7	9.4	89.9		

150 μm reaches 98.6%, and there are almost no particles smaller than 150 μm, thus achieving the purpose of pre-classification, which reduces the load for the subsequent dynamic rotor classifier.

As can be seen from the table, the coarse powder recovery rate increases significantly and the fine powder recovery rate decreases gradually as the rotor cage speed increases. This can be explained that with the increase in the rotor cage speed, the centrifugal force on the particles in the classification area increases, resulting in more coarse particles being collected. The main reason for the decrease in the fine powder recovery rate is the collision and agglomeration between particles, coupled with the increase in the centrifugal force on particles, some fine particles mistakenly report to the total coarse fraction.

It can also be obtained from the table that the average recovery rate of the fine powder calculated is 97.2%, which shows a good result for collecting the fine powder. When the rotor cage speed is 300 rpm, the classification effect for the coarse powder is better with 90.5% of the coarse powder recovery rate and the content of particles smaller than 150 μm in the coarse fraction is only 5%. This indicates that while maintaining a high coarse powder recovery rate, the coarse fraction contains very little fines, thus ensuring production efficiency. When the rotor cage speed is 500 rpm, the classification effect for the fine powder remains best with 91.8% of the fine powder recovery rate, and the content of particles larger than 75 μm in the fine fraction is only 10.1%. It illustrates that the purity of the finished product is higher at this speed, and it also shows that the classification effect of particles larger than 75 μm is more effective at high speeds. The samples for the coarse, medium-coarse, and fine fractions are obtained at the speed of 500 rpm, as shown in fig. 14.

Figure 14. Material samples at *n* = 500 rpm; (a) coarse fraction, (b) medium-coarse fraction, and (c) fine fraction

Figures 15(a) and 15(b) indicate the particle size distribution and classification efficiency curves of fine powder group under two operating conditions. Compared to the rotor cage speed of 300 rpm, the fine fraction at the speed of 500 rpm has a smaller particle size composition and a narrower particle size distribution. The classification efficiency is expressed as the amount of a particular size fraction of the materials reporting to the fine fraction. As seen in fig. 15(b), the cut size is 116.3 μm and 68.9 μm for the speed of 300 rpm and 500 rpm, respectively. In addition, the classification efficiency curve is steeper at the speed of 500 rpm, indicating a higher classification accuracy with a satisfactory value of 0.64, which shows that the increase in the rotor cage speed can significantly improve the classification performance.

Conclusions

In the present study, a three-separation combined air classifier designed based on two key aspects of material dispersion and classification was introduced. The classifier has been

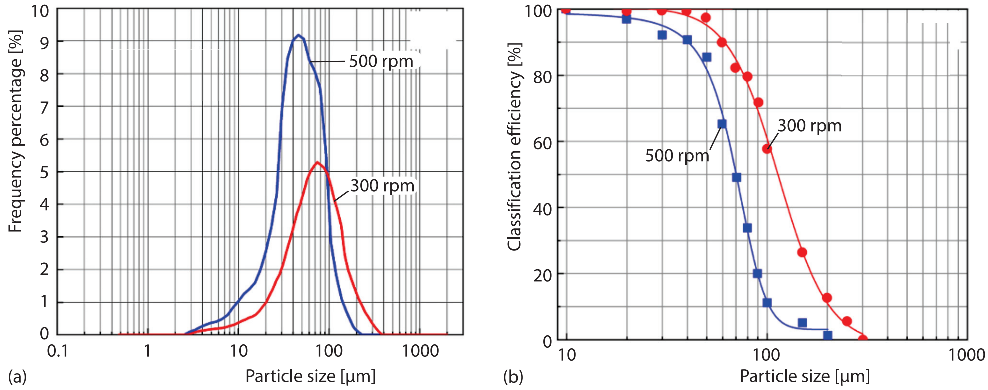

Figure 15. Fine fraction particle size distributions (a) and classification efficiency curves (b)

numerically simulated and experimentally studied. The purpose of completing the simulation is to visualize the flow field properties and particle motion that cannot be observed in experiments. The conclusions are as follows.

- Air and materials first enter the V-classifier for pre-classification and pre-dispersion, which effectively solves the problems of uneven material dispersion and high dust concentration in the turbo air classifiers, and provides more possibilities for high-efficient classification. Moreover, the load on the dynamic rotor classifier part is reduced.
- The high speed rotation of the rotor cage provides tangential velocity for the air-flow in the classification zone, which is small in the classification zone. However, as it enters the rotor channel, the tangential velocity of the air-flow increases steadily and remains stable in the axial direction, providing a stable centrifugal force field for material classification.
- According to the analysis of the flow field and particle trajectory, the classification chamber and cone part can be divided into particle upward region and coarse particle downward region, and the interface between the two regions is relatively clear.
- The content of the coarse powder classified by the V-classifier is up to 98.6%, which proves that it has a good pre-classification effect. In this experiment, the best classification effect of the fine powder is achieved when the rotor cage speed was 500 rpm, and the recovery rate of fine powder reaches 91.8%. Meanwhile, the classification accuracy reaches 0.64. When the rotor cage speed is 300 rpm, the coarse powder has the best classification effect with a 90.5% coarse powder recovery rate.

Acknowledgment

This work was supported by the Priority Academic Program Development of Jiangsu Higher Education Institutions (PAPD).

Conflict of interest

The authors declare no financial or commercial conflict of interest.

References

[1] Feng, Y., *et al.*, Effects of Operating Parameters on Flow Field in a Turbo Air Classifier, *Minerals Engineering*, *21* (2008), 8, pp. 598-604
[2] Li, H., *et al.*, Introduction Vertical and Horizontal Rotor Separators, *Cement*, *42* (2015), 12, pp. 31-36
[3] Barimani, M., *et al.*, Particulate Concentration Distribution in Centrifugal Air Classifiers, *Minerals Engineering*, *126* (2018), Sept., pp. 44-51

[4] Ren, W., *et al.*, Design of a Rotor Cage with Non-Radial Arc Blades for Turbo Air Classifiers, *Powder Technology*, *292* (2016), May, pp. 46-53
[5] Zhao, H., *et al*., Effects of the Impeller Blade Geometry on the Performance of A Turbo Pneumatic Separator, *Chemical Engineering Communications*, *205* (2018), 12, pp. 1641-1652
[6] Jiang, D., Tao, R., Study of the effect of O-Sepa Separator Blade Structure on the Flow Field in the Classification Zone, *Mechanical Engineering and Automation*, (2014), 06, pp. 22-23+26
[7] Yu, Y., *et al*., A New Volute Design Method for the Turbo Air Classifier, *Powder Technology*, *348* (2019), Apr., pp. 65-69
[8] Liu, R., *et al.*, Effects of Axial Inclined Guide Vanes on a Turbo Air Classifier, *Powder Technology*, *280* (2015), Aug., pp. 1-9
[9] Huang, Q., *et al.*, Turbo Air Classifier Guide Vane Improvement and Inner Flow Field Numerical Simulation, *Powder Technology*, *226* (2012), Aug., pp. 10-15
[10] Ren, C., *et al*., Effect of Air Guide Vanes on The Flow Field in A Vortex Air Classifier, *Chemical Progress*, *38* (2019), 09, pp. 3988-3994
[11] Guo, L., *et al*., Flow Field Characteristics of the Rotor Cage in Turbo Air Classifiers, *Chinese Journal of Mechanical Engineering*, *22* (2009), 3, pp. 426-432
[12] Liu, R., *et al*., Study of Matching the Inlet Air Speed and Rotating Cage Speed of a Vortex Air Classifier, *Chemical Engineering*, *43* (2015), 03, pp. 41-45
[13] Li, B., *et al*., Development and Application of DS-M Type Ultra-Subdivisional Sorting Machine, *Cement Engineering*, (2020), 03, pp. 33-35
[14] Li, H., *et al*., O-Sepa Vortex Separator Structural Features And Improved Design, *Journal of Sichuan Institute of Technology (Natural Science Edition)*, (2007), 01, pp. 15-19
[15] Sun, J., *et al*., Structural Analysis and Improvement of the O-Sepa Powder Separator, *Cement*, (2013), 02, pp. 35-37
[16] Sun, J., Jiang, D., Analysis of the Flow Field of the O-SEPA Separator and Its Effect on Performance, *Journal of Yancheng Engineering College (Natural Science Edition)*, *21* (2008), 04, pp. 38-41
[17] Lin, Y., *et al.*, Exploring the Factors Affecting the Efficiency of the O-Sepa Separator, *China Cement*, (2020), 07, pp. 95-97
[18] Wu, S., *et al*., Design of a New Double Layer Spreading Plate for A Turbo Air Classifier, *Powder Technology*, *312* (2017), May, pp. 277-286
[19] Xu, H., Improvement of Unreasonable Air Inlet Duct Arrangement of O-Sepa Separator, *Cement*, (2012), 10, pp. 61-62
[20] Zhao, D., Zhang, S., Influence of O-Sepa Separator Worm Shell Structure on Classification Performance, *China Powder Technology*, *21* (2015), 06, pp. 20-24
[21] Jia, F., *et al*., A New Rotor-Type Dynamic Classifier: Structural Optimization and Industrial Applications, *Processes*, *9* (2021), 6, 1033
[22] Mou, X., *et al*., CFD-Based Structural Optimization of Rotor Cage for High-Efficiency Rotor Classifier, *Processes*, *9* (2021), 7, 1148
[23] Li, Q., *et al*., Effects of a Guide Cone on the Flow Field and Performance of a New Dynamic Air Classifier, *Processes*, *10* (2022), 5, 874
[24] Kundu, T., *et al*., Performance Evaluation of the VSK Separator for Treating Mineral Fines, *Minerals Engineering*, *167* (2021), 106883
[25] Guizani, R., *et al*., Effects of the Geometry of Fine Powder Outlet on Pressure Drop and Separation Performances for Dynamic Separators, *Powder Technology*, *314* (2017), June, pp. 599-607
[26] Sun, Z., *et al*., Experimental and CFD Study on a Cyclonic Classifier with New Flow Pattern, *Advanced Powder Technology*, *30* (2019), 10, pp. 2276-2284
[27] Dijkink, B. H., *et al*., Air Dispersion of Starch-Protein Mixtures: A Predictive Tool for Air Classification Performance, *Powder Technology*, *172* (2007), 2, pp. 113-119
[28] Diao, X., *et al*., Numerical Simulation of Particle Dispersion in the Feed Tube of an Ultrafine Classifier, *Journal of East China University of Science and Technology (Natural Science Edition)*, *38* (2012), 02, pp. 252-258
[29] Tong, C., *et al*., Analysis of the Effect of Vertical Mill Blade Structure on the Velocity Field in the Classification Zone, *Chemical Progress*, *31* (2012), 04, pp. 778-783

Paper submitted: May 13, 2023
Paper revised: July 29, 2023
Paper accepted: August 2, 2023